Green Chemistry

Accepted Manuscript

ROYAL SOCIETY OF CHEMISTRY

www.rsc.org/greenchem

Green Chemistry

RSCPublishing

ARTICLE

024Cite this: DOI: 10.1039/x0xx00000x

Received 00th January 2012,
Accepted 00th January 2012

DOI: 10.1039/x0xx00000x

www.rsc.org/

Producing hierarchical porous carbon monoliths from hydrometallurgical recycling of spent lead acid battery for application in lithium ion batteries

Xiong He[a], Xiaoyu Peng[a], Yuxuan Zhu[b], ChaoLai[b]*, Caterina Ducati[a], R.Vasant Kumar[a]*

In this paper, an environmentally clean process to recycle the paste from a spent lead acid battery (LAB) is further developed in order to produce a porous carbon anode material for a lithium ion battery (LIB) which is currently in increasing focus as the solution for future energy storage and distribution network. Using lead citrate from hydrometallurgical leaching of lead paste as a precursor, electrochemically active carbon materials were produced as a new product with hierarchical open sponge-like porosity. It was found that anode materials made from porous carbon by pyrolysing lead citrate at 500°C, with high micropore (<2nm) volume (0.0248cm^3/g) and BET surface area (138.5m^2/g), showed remarkable reversible capacity values beyond intercalation at both low and high current densities. In particular, at the high current density of 5000 mA g-1 (13.4C, according to the theoretical capacity of 372 mAh g-1), a high discharge capacity of 217mAh g-1 was maintained even after 200 cycles, much superior in comparison with other carbon materials.

Introduction

Sustainable and renewable energy solutions are receiving great attention. Researchers are seriously engaged in exploring new technologies related to environmental and energy issues. This paper is directly concerned with both a green recycling technology and energy storage materials.

Due to the rapid development of automobile industry, LAB production has dramatically increased during the past few years[1]. In 2013, around 11 million metric tons of refined lead was produced, of which 80% is used in LABs (http://www.ilzsg.org/static/enduses.aspx?from=12). Moreover, LABs are also widely used in many other fields, such as HEVs, backup power supply and grid energy storage for wind and solar power plants. The growth in LAB production has increased the pressure on the lead recycling sector. Currently, most of the spent LABs are recycled by using pyro-metallurgical process, which are associated with environmental issues arising from lead dust and sulphur dioxide emission[2]. Therefore, hydro-metallurgical processes are increasingly studied to avoid the high temperature dependent pollution[3–5]. The new processes can help to reduce dust and acid pollution by the removal of sulphur through leaching and avoidance of lead fuming from the low operating temperature. Citrate chelation has been proved to be effective for desulphurization of spent lead acid battery paste, while simultaneously fixing lead in lead citrate crystals.[6] Lead citrate crystal is a versatile raw material from the new process as it can be readily combusted in air at relatively low temperatures (below lead fuming temperatures) to produce leady oxides for making new batteries and/or pyrolysed in absence of oxygen to produce metallic lead and highly active carbon for new applications.

The main concern is the currently relatively high price of sodium citrate reagent which makes the operating costs less economically friendly for recycling LABs[7]. Therefore, the process should be tailored to be economically more viable, by producing a high value electrochemically active carbon from a proportion of the lead citrate.

Highly active carbon materials have been widely used in energy-related applications (supercapacitor, lithium ion battery (LIB), lithium sulphur battery, gas storage).[8,9] Especially in LIBs, carbon materials in many forms such as graphite/graphitized carbon, CNTs, graphene and amorphous carbon has been proved to be the primary choice for the anode material[10] due to its useful chemical and physical properties. Carbon materials have been widely used in battery industry. As anode materials for LIBs, graphite, one-dimensional (1D), two-dimensional (2D) and porous carbon have been explored. Graphite has a limited theoretical capacity of 372 mAh g^{-1} by forming stoichiometry LiC_6. Nanostructured carbon materials, such as carbon nanotubes (CNTs), including single wall carbon nanotube (SWCNT) and multiwall carbon nanotube (MWCNT), carbon nanofibres (CNFs), graphene and porous carbon with various pore sizes can improve electrochemical performance due to their special structures and morphologies. 1D nanostructured carbons obtain high Coulombic efficiency and good cycling stability, but poor rate performance and low volumetric energy density. Graphene carbons have good rate capability but low initial Coulumbic efficiency and large irreversible capacity. Porous nanostructured carbons which combine both the advantages of nano and micro are more attractive.[11] Similar to LIBs, Na-ion batteries (NIBs) can also take advantages of carbon materials.[12] Acting as part of the cathode materials of lithium sulfur batteries (LSBs), nanostructured carbon materials can also contributes to future energy storage solutions.[13] Nanostructured porous carbon materials which have outstanding physical and chemical properties are of great importance in the battery industry. Among all the carbonaceous materials, 3D amorphous porous carbon with different range of pore size meets the requirements for LIB anode materials best by providing robust mechanical strength and high reversible specific capacity.[11] Porous carbon can be classified as microporous (<2nm), mesoporous (2-50nm) and macroporous (>50nm) based on its average pore size. Many methods have been developed to synthesize porous carbon obtaining different pore size and pore size distribution range[9,14]. These include synthesis of uniform porous carbon by using: Zeolite Y template,[15] silica template[16] and anodic aluminum oxide templates,[17] and hierarchical porous carbon from various precursors, such as polymers, copolymers and biomass.[9] Some researchers have tried to utilize waste materials, food, agriculture waste and insects as the source of carbon.[18] Developing low-cost and environmental-friendly process of synthesizing functional carbon with excellent properties is also increasingly popular.

In this work we demonstrate the synthesis of hierarchical porous carbon materials as a co-product from a novel environmental-friendly hydrometallurgical LAB recycling process. We have examined the properties of the derived carbon for LIB applications. Lead sulphate, the main component of paste from spent LABs, was used as starting lead-containing raw material. According to previous study,[19] spent LAB paste is a complex mixture of lead sulphate, lead oxides and metallic lead. The lead sulphate in spent LAB paste is identical in structure to pure lead sulphate. The structure of the lead citrate produced from spent LAB paste and pure chemicals is also the same. So we reasonably choose pure lead sulphate here to simulate spent LAB paste. By leaching lead sulphate with sodium citrate/citric acid buffer solution at room temperature, desulphurization was completed by transferring all lead into lead citrate precursors which were then converted to a lead-carbon composite after low temperature calcination (pyrolysis) at 500°C in Ar or N_2. Lead was recovered from the lead-carbon composite with nitric acid to transfer lead into an aqueous solution from which lead can be recovered by electrowinning. Thus from the composite, porous carbon is recovered as the remaining phase as an important co-product of this process. Hierarchical porous carbon was then characterized and demonstrated to be a suitable host for lithium as an anode material for a LIB.

Experimental

Materials and Methods

The novel LAB recycling process using leaching/desulphurization with citric acid system and electrowinning is schematically described in Fig. 1, with the additional incorporation of pyrolysis to synthesize hierarchical porous carbon for LIB anode materials. The green dash line arrows indicate experiments proposed but not included in this paper. Those investigated and reported in this paper are desulphurization process, thermal process, porous carbon isolation process and LIB preparation and testing. Since lead sulphate is the major component in a spent LAB paste, and also the most difficult component to recover or transform,[6] pure lead sulphate, was used to simulate spent LAB paste.

Preparation of lead citrate precursors

Preparation of lead citrate precursors, also the desulphurization of lead sulphate (trace metals basis, 99.995%), was conducted by following a modified previously reported method.[5] 10g of lead sulphate powder was added to 50mL citric acid (citric acid monohydrate, ACS reagent, ≥99.0%) and sodium citrate (sodium citrate tribasic dehydrate, ACS reagent, ≥99.0%) solution (pH 5.4, 1.98 M). Citric acid acts as the pH buffer to obtain the optimal lead recycling efficiency. Leaching experiments were then conducted in a 250 mL glass beaker with constant magnetic stirring at 30°C for 6 hours (although 2 hours has been proved long enough for complete desulphurization). After leaching, the precipitated solids were filtered, washed with distilled water and dried at 90°C for 12 hours to obtain lead citrate crystals.

Preparation of hierarchical porous carbon material

The lead citrate crystalline powder was then pyrolyzed in absence of air at selected temperatures of 350, 500 and 800°C in flowing argon (at 50mL/min) for 1 hour. The resulting product which was shown to be a lead-carbon composite was carefully collected then reacted with 1M nitric acid solution for 6 hours at 40°C to isolate porous carbon while dissolving lead. The remaining black paste was then washed with distilled water and centrifuged to obtain a black mass found to be carbon with a hierarchical porous structure (Fig.2). The as

prepared hierarchical porous carbon, after drying in an oven was then tested as anode host material for a LIB.

Preparation of and electrochemical testing of the anodes

The working electrodes were prepared by compressing a mixture of the active materials, acetylene black, and binder (polytetrafluoroethylene, PTFE) in a weight ratio of 70:20:10. The carbon anodes were cut into wafer with diameter of 8mm and the loading is 3.6-4 mg cm^{-2}. Lithium metal was used as the counter and the reference electrode. The electrolyte was $LiPF_6$ (1 M) dissolved in a mixture of ethylene carbonate (EC), ethyl methyl carbonate (EMC) and dimethyl carbonate (DMC) with a volume ratio of 1:1:1[20,21]. Pouch type half-cells were used to test the electrochemical properties of the active materials. LAND-CT2001A galvanostatic test equipment was employed to measure electrochemical capacity and cycle life at room temperature of the working electrodes at selected values of current densities of 100, 1000 and 5000 mA g-1. The cut-off potentials for charge and discharge were set at 3.0 and 0.05 V (vs. Li+/Li), respectively.

Characterizations

The phase composition of the lead citrate crystalline powder and porous carbon were investigated by using Bruker D8-advanced powder X-ray diffractometer with Cu Kα radiation (40kV, 40mA). Microstructure of samples was observed with FEI Nova NanoSEM and FEI Tecnai F20 FEGTEM. Nitrogen adsorption-desorption isotherms were measured on a Micrometrics ASAP 2020 instrument. The Brunauer-Emmett-Teller (BET) surface area was estimated over a relative pressure (P/P_0) range of 0.01-0.20. The pore size distribution and pore volume was estimated from the analysis of the adsorption branches of the isothermal using the Barrett-Joyner-Halenda (BJH) method. The t_{HJ}-plot micropore volume is calculated using Harkins and Jura method. Raman data were obtained on a Dilor XY-800 spectrometer, using 514nm wavelength laser. Thermal gravimetric analysis (TGA) was conducted on a TA Instruments Q2000 thermal analyzer in argon and air with a heating rate of 10 ^oC min^{-1}.

Results and discussion

Synthesis of lead citrate precursors

In the desulphurization process, lead sulphate reacts with free citrate ions in the solution by forming $Pb_3(C_6H_5O_7)_2{\cdot}3H_2O$ as white precipitate. The reaction between $PbSO_4$ and $Na_3C_5H_5O_7{\cdot}2H_2O$ followed the reaction (1).[7,22]

$$3PbSO_4 + 2Na_3(C_6H_5O_7){\cdot}2H_2O \rightarrow Pb_3(C_6H_5O_7)_2{\cdot}xH_2O + 3Na_2SO_4 + (4-x)H_2O \quad (1)$$

According to previous reported results[5,6], complete desulphurization of lead sulphate can be completed within 2 hours at room temperature. Here the leaching time was extended to 6 hours, and leaching temperature was kept at 30^oC, in order to ensure complete absence of any unreacted lead sulphate in the lead citrate precursor.

SEM figure (Fig.3a) of the lead citrate displayed a thin plate like structure (less than 5μm in length). Although the lead citrate precursors seemed well crystalized in the SEM image, the XRD spectra (Fig.3b) indicated relatively poorly crystallized pattern with only one sharp peak at 2θ=8.95^o and two broad peaks at around 2θ=27^o and 42^o. Previous reports have shown different types of lead citrates can form ranging from the highly crystalline lead mono citrate to low crystallinity lead tri-citrate the latter being produced in this leaching process for which there is no standard PDF card as yet available for this pattern. The one sharp peak can be allocated to $Pb_3(C_6H_5O_7)_2{\cdot}3H_2O$ which is known to have one strong peak at around that range.[7] No lead sulphate peaks were observed.

Thermal decomposition of lead citrate precursors

TGA/DSC curves of the lead citrate precursor are shown in Fig.4. There are three stages of weight loss during the decomposition in absence of air (N_2 was used). The first weight loss stage started from about 170 ^oC can be assigned to dehydration and loss of water of crystallization. The broad DSC peaks at around 200-270 ^oC indicate complex decomposition reactions. The next sharp DSC peak at around 350 ^oC and the corresponding drastic mass loss (14.15 wt %) can also be ascribed to lead citrate decomposition. No further mass loss stage after the completion of the endothermic process at around 350 ^oC is observed, which is taken as an indication of termination of lead citrate decomposition. The total mass loss at 500 ^oC is 32.9 wt%, which corresponds well with the theoretical mass loss of 33.6 wt%[23]. The mass loss curve then remains stable until 800 ^oC with only a gradually slowly decrease arising most probably from evaporation of lead. The total mass loss at 800 ^oC is 34.8 wt%. Another significant mass loss stage starts from around 850 ^oC which is considered as arising from increased lead evaporation. In order to select the optimal calcination temperature, two further thermal analyses have also been conducted with heating temperatures up to 350 ^oC and 500 ^oC. Based on the thermal analysis results, three different calcination temperatures (350, 500 and 800 ^oC) were chosen to produce porous carbon materials.

According to Brown's research report[23], pyrophoric lead and carbon are the final products of lead citrate decomposition in inert gas atmosphere with a weight loss of around 33.6 wt%. The proposed reaction was described as:

$$Pb_3(C_6H_5O_7)_2{\bullet}3H_2O(s) \rightarrow [3Pb+7.5C](s)+5H_2O(g)+4.5CO_2(g) \quad (2)$$

The most common thermal decomposition products are Pb (labeled with blue arrows) and C, shown in Fig. 5c and the mixture also consists of some PbO (labeled with black arrow). The presence of lead oxides has mainly resulted from the oxidation of nano-sized pyrophoric lead particles. While the lead particles were oxidized to lead oxides, the carbon monolith and its surface area would be expected to remain unchanged.[24–26] According to the TGA analysis, it is reasonable to assume that the decomposition process is following the above equation. The loss of carbon in the following collecting process can be neglected. Then the carbon yield of the lead citrate decomposition process is 8.5 %. The SEM images are shown in Fig.5a&b. As displayed in the SEM images, the product consisted of numerous isolated round lead particles with a wide size range distributed on the carbon matrix. The maximum particle size of lead metal is around 50 nm. Some of the lead metal particles were partially adhered in carbon, some were attached on the surface of carbon and some were fully located inside carbon particles. The

particle size of some of the lead particles is very small (<50 nm). According to Feitknecht's research, lead metal with surface area higher than 3 m^2/g will have pyrophoric behavior.[23] Then the as prepared lead particles will be expected to have pyrophoric behavior. To obtain as much as carbon as possible, the decomposition products should be transferred into next step as soon as possible from argon protected furnace preventing from exposure to air. Fig.5d shows the TEM image of lead carbon composite. The black particles in the image are lead. As indicated by the color differences inside the particles, the round lead spheres with above 20 nm diameters are not uniform but more likely to be formed by agglomeration of smaller lead particles.

Characterization of porous carbon

Fig.6a shows the Raman spectra of carbon produced from lead citrate precursor at three different decomposition temperatures (350, 500 and 800 ^oC). Fundamental vibrations of D bands (the A_{1g} symmetry mode, disorder) in the vicinity of 1320 cm^{-1} and G bands (the E_{2g} mode of the sp^2 carbon atoms, graphite) in the vicinity of 1590 cm^{-1} were clearly observed for the obtained carbon materials. As the annealing temperature increases from 350^{o}C to 800 ^{o}C, the intensity ratio of D-band and G-band, I(D)/I(G), increases from 0.70 to 1.19, suggesting higher content of disorder in carbon sheets.[27–29] More disordered structure can offer more active sites for lithium-ion storage.Fig.6b shows the XRD patterns of the same carbon materials. The two broad peaks at around 2theta=23.5^o and 42.5^o , which correspond to (0 0 2) and (1 0 0) reflections, denote disordered graphitic carbon.[18,30] There is no other impurity peak, such as lead, indicating the complete removal of metal residues. This also can be further confirmed by the TGA curves of porous carbon in Fig. S1. As presented, the weight loss can reach to 100% before 500 ^{o}C in air.

SEM images of the porous carbon material, Fig.7a and Fig.7b, display a surface morphology characterized by craters with different diameters and depth. The diameter of the craters, which ranges from 2 to 50 nm, matches well with the size of the lead metal showed in Fig.5a,b. The carbon bulk shows a curved surface, which results from the constraining force during the pyrolysis.[23] The HR-TEM images in Fig.7c,d,e show a hierarchical, open 3D-porous morphology which indicates the existence of varying size of pores inside the carbon matrix as well, which is evidently proved by the overlap of the pores. The whole carbon matrix looks more like a piece of micro-sized sponge. The pores located inside carbon matrix also have similar diameters as the surface craters, as indicated in Fig.7d. In accordance with XRD and Raman results, HR-TEM also reveals a disordered structure, Fig.7f.

Energy dispersive X-ray spectrometry (EDX) mapping analysis is also conducted to investigate the surface element state of porous carbon. As shown in Fig. S2, the overlapped element mapping indicates the homogeneous distribution of carbon and oxygen on the surface of the porous carbon. The EDS spectrum in Fig. S3 obtained from the same region of the sample confirms the presence of oxygen atoms. There are no lead peaks detected, consistent with the results of TGA. To further illustrate the content of existing state of carbon and oxygen, XPS spectrums are given in Fig.8. XPS survey scan in Fig. 8a confirm the presence of carbon and oxygen atoms in the porous carbon, and there are no obvious difference for the carbon materials calcined at different temperature, except that the oxygen content increases from 13.52 at% to 15.75 at% and 14.33 at% as the annealing temperature increases from 350^{o}C to 800^{o}C. Fig. 8b is the the XPS core level spectra of C1s of the sample obtained at 500 ^{o}C. The peaks centred at 284.4 and 284.9 eV can be attributed the C=C/C-C groups.[31,32] The peaks centred at 285.8 and 286.9 eV are related to the C-O epoxy and hydroxyl groups, while the peaks at 288.4 and 289.2 eV are designated as C=O carbonyl groups and O=C-O carboxyl groups.[32] There are no obvious peaks of lead detected (below 0.13 at%), consistent with above characterizations. The formation of C-O and C=O groups is also can be further confirmed by the FTIR spectrum in Fig. S4.

The N_2 sorption isotherms and the BJH pore size distribution of porous carbon produced at three different temperatures are shown in Fig.9. As shown in Fig.9a, all the isotherms exhibit a typical IV isotherm, with an obvious hysteresis loop, indicating the existence of mesoporous structure.[18] Point B, labeled with a blue arrow, indicates the completion of monolayer coverage and the start of multilayer adsorption.[33] These hysteresis loops can be categorized as H4 type, which indicates absence of large mesopores embedded in monolith with smaller pores.[34] The presence of low pressure hysteresis, especially obvious in 500^{o}C carbon, indicates the existence of micropores in the carbon materials. This may also indicate a non-rigid porous structure which results in the swelling of the absorbent.[33] The steep fall of desorption branch at lower limit of hysteresis indicates the existence of disordered domains resulting from collapse of lamellar structure, which matches the SEM results (Fig.5a&b). As shown in Fig. 9a, high temperature annealed carbon possess bigger hysteresis lop, which indicates the larger mesopore volume. At point B and final adsorption stage, high temperature carbon (500^{o}C and 800^{o}C) absorbed more N_2, which manifests larger outside surface area. The PSD (pore size distribution) pattern (Fig. 9b) and the quantitative results (Table. 1) provide further verification. As indicated by the more obvious low pressure hysteresis loop and higher BJH adsorption at smaller pore size (2-5 nm), porous carbon produced at 500^{o}C gives a larger BET surface area of 138.5 m^2g^{-1}, a larger micropore volume of 0.0248 cm^3g^{-1} and a smaller average pore size of 15.1nm. The decrease of micropore volume, concurrently the increase of mesopore volume, at 800^{o}C in comparison with 500^{o}Csamples may result from the coalescing of lead metals at the smaller size.

Battery test results

Porous carbon has been widely used in many energy and environment related areas, such as in supercapacitors, batteries, and hydrogen storage. In this paper, LIB batteries application, as one of the possible applications of this as-prepared porous carbon materials are considered. The electrochemical performance of the carbon material, prepared as a working

electrode as described in the experimental section, was firstly tested in a half cell using lithium metal as the counter electrode. The initial discharge-charge curves at the current density of 100 mA g^{-1} are presented in Fig. 10a. As shown, all the samples display similar sloping discharge curves, which is a typical feature for carbon materials with a low degree of graphitization.[35] The plateau between 0.5-0.9V can be attributed to the formation of the solid electrolyte interphase (SEI) film arising from the decomposition of the electrolyte. The sample thermally treated at 350 ^{o}C, shows a high discharge capacity of 620.9 mAh g^{-1} (per g of active materials), but a very low charge capacity of 137.5 mAh g^{-1}, indicating that the activation process at this temperature is not sufficient for applications in Li-ion batteries. When the higher temperature was used, a significant increase of the initial capacity can be observed. The initial discharge-charge capacity is 1629.1 and 849.7 mAh g^{-1}, respectively, for the samples treated at 500 ^{o}C, while it is 1233.3 and 676.4 mAh g^{-1} for the sample treated at 800 ^{o}C. The large irreversible capacity and low initial coulombic efficiency (350 ^{o}C:22.1%; 500 ^{o}C:52.1%; 800 ^{o}C:54.8%) mainly result from the formation of SEI layer and irreversible lithium insertion sites within the porous carbon material.[26] Fig. 10b shows the cycle curves of the samples obtained at different temperatures at the current density of 100 mA g^{-1}. As illustrated, the carbon materials obtained at 500 ^{o}C present the highest reversible capacity, and after 50 cycles, the discharge capacity can be retained at 669.0 mAh g^{-1}, which is much higher than the theoretical capacity of graphite anodes, suggesting that some of the very fine pores can act as storage for metallic Li, or that the surface storage of very active C is much higher than the intercalated Li in bulk graphite. For the samples obtained at 350 and 800 ^{o}C, the reversible capacity after 50 cycles is just about 478.3 and 138.7 mAh g^{-1}. The enhanced electrochemical performance of the samples obtained at 500 ^{o}C can be attributed to its unique porous structure. As compared to the carbon obtained at 350 ^{o}C, higher thermal-treated temperature can offer better conductivity. However, when the temperature increase to 800 ^{o}C, it will destroy its porous structure (Table 1) which is important to facilitate fast transport of electrolyte ions. Therefore, the porous carbon treated at 500 ^{o}C presents the best electrochemical performance. Furthermore, the oxygen doping and its disorder structure can give more active sites for Li^{+} storage or adsorption, which leads to a higher reversible capacity than graphite.[37] Fig. 9c shows the initial discharge-charge curves of the samples treated at 500 ^{o}C at different current densities. At the current density of 1000 mAg^{-1}, a high capacity of 843.1 mAh g^{-1} can be obtained, and still can be retained at 677.9 mAh g^{-1} when the current density increasing to 5000 mA g^{-1}. The cycling curves of the carbon materials obtained at 500 ^{o}C are shown in Fig. 9d. As shown, excellent cycle performance can be observed. At the current density of 1000 mA g^{-1}, the discharge capacity can be retained at 289.5 mAh g^{-1} after 200 cycles. Moreover, when the current density increasing to 5000 mA g-1 (13.4C, according to the theoretical capacity of 372 mAh g^{-1}), high discharge capacity of 216.7 mAh g^{-1} still can be obtained after 200 cycles, which is a very competitive result as compared other carbon materials,[38–40] and the capacity retention can reach up to 74.9% as compared to that at the current density of 1000 mA g^{-1}. These electrochemical tests suggest that the carbon materials obtained from recycling waste materials of lead-acid batteries are promising anodes material with high capacity and excellent rate performance.

Conclusions

Hierarchical mesoporous carbon materials were successfully produced as a side product in a novel green hydrometallurgy LABs recycling process. In this process, lead-containing parts in the spent lead acid battery paste were transferred to lead citrate precursor. Then by heat treatment and acid wash treatment, lead can be recycled from solution. Porous carbon was then collected as side-product. The resulting carbon materials have a sponge-like open porosity. High capacity and excellent rate performance was achieved when used as anode material in LIBs. Further optimization of the process and further application of the carbon materials is still in need of more research. Nevertheless, this study has already proved that hierarchical porous carbon produced from this novel hydrometallurgy LABs recycling process provides considerable potential as anode material for high-rate LIBs.

Acknowledgements

X.P. and C.D we acknowledge funding from the ERC, under grant number 259619 PHOTO EM.

Notes and references

[a]. Department of Materials Science and Metallurgy, University of Cambridge, 27 Charles Babbage Rd, Cambridge, UK, CB3 0FS.
Email: xh253@cam.ac.uk, rvk10@cam.ac.uk,
Tel: +44 01223 331951
[b]. School of Chemistry and Chemical Engineering, and Jiangsu Key Laboratory of Green Synthetic Chemistry for Functional Materials, Jiangsu Normal University, Xuzhou, Jiangsu 221116, P. R. China,
Email: laichao@jsnu.edu.cn
* The corresponding author

Electronic Supplementary Information (ESI) available: [details of any supplementary information available should be included here]. See DOI: 10.1039/b000000x/

1. L. Chen, Z. Xu, M. Liu, Y. Huang, R. Fan, Y. Su, G. Hu, X. Peng, and X. Peng, *Sci. Total Environ.*, 2012, **429**, 191–198.

2. M. a. Kreusch, M. J. J. S. Ponte, H. a. Ponte, N. M. S. Kaminari, C. E. B. Marino, and V. Mymrin, *Resour. Conserv. Recycl.*, 2007, **52**, 368–380.

3. M. S. Sonmez and R. V. Kumar, *Hydrometallurgy*, 2009, **95**, 53–60.

4. J. Pan, Y. Sun, W. Li, J. Knight, and A. Manthiram, *Nat. Commun.*, 2013, 4, 2178.

5. M. S. Sonmez and R. V. Kumar, *Hydrometallurgy*, 2009, **95**, 82–86.

6. L. Li, X. Zhu, D. Yang, L. Gao, J. Liu, R. V. Kumar, and J. Yang, *J. Hazard. Mater.*, 2012, **203-204**, 274–282.

7. X. Zhu, X. He, J. Yang, L. Gao, J. Liu, D. Yang, X. Sun, W. Zhang, Q. Wang, and R. V. Kumar, *J. Hazard. Mater.*, 2013, **250-251**, 387–96.

8. M. Sevilla and R. Mokaya, *Energy Environ. Sci.*, 2014, **7**, 1250–1280.

9. S. Dutta, A. Bhaumik, and K. C.-W. Wu, *Energy Environ. Sci.*, 2014, **7**, 3574–3592.

10. L. Ji, Z. Lin, M. Alcoutlabi, and X. Zhang, *Energy Environ. Sci.*, 2011, 4, 2682–2699.

11. P. Roy and S. K. Srivastava, *J. Mater. Chem. A*, 2015, **3**, 2454–2484.

12. M. H. Han, E. Gonzalo, G. Singh, and T. Rojo, *Energy Environ. Sci.*, 2015, **8**, 81–102.

13. J. Zhou, R. Li, X. Fan, Y. Chen, R. Han, W. Li, J. Zheng, B. Wang, and X. Li, *Energy Environ. Sci.*, 2014, **7**, 2715–2724.

14. J. Lee, J. Kim, and T. Hyeon, *Adv. Mater.*, 2006, **18**, 2073–2094.

15. Z. Ma, T. Kyotani, Z. Liu, O. Terasaki, and A. Tomita, *Chem. Mater.*, 2001, **13**, 4413–4415.

16. S. Che, A. E. Garcia-Bennett, X. Liu, R. P. Hodgkins, P. A. Wright, D. Zhao, O. Terasaki, and T. Tatsumi, *Angew. Chemie Int. Ed.*, 2003, **42**, 3930–3934.

17. G. Che, B. B. Lakshmi, E. R. Fisher, and C. R. Martin, *Nature*, 1998, **393**, 346–349.

18. M. Biswal, A. Banerjee, M. Deo, and S. Ogale, *Energy Environ. Sci.*, 2013, **6**, 1249–1259.

19. X. Zhu, L. Li, X. Sun, D. Yang, L. Gao, J. Liu, R. V. Kumar, and J. Yang, *Hydrometallurgy*, 2012, **117-118**, 24–31.

20. L. Ji, Z. Lin, A. J. Medford, and X. Zhang, *Carbon N. Y.*, 2009, **47**, 3346–3354.

21. Y. S. Hu, P. Adelhelm, B. M. Smarsly, S. Hore, M. Antonietti, and J. Maier, *Adv. Funct. Mater.*, 2007, **17**, 1873–1878.

22. J. Yang, R. V. Kumar, and D. P. Singh, *J. Chem. Technol. Biotechnol.*, 2012, **87**, 1480–1488.

23. M. E. Brown, *J. Chem. Soc. Faraday Trans. 1*, 1973, 69, 1202–1212.

24. P. E. Yankwich and J. L. Copeland, *J. Am. Chem. Soc.*, 1957, **79**, 2081–2086.

25. J. Charles, P. Kopf, and S. Toby, *J. Phys. Chem.*, 1966, **350**, 1478–1482.

26. T. Gorrie, P. Kopf, and S. Toby, *J. Phys. Chem.*, 1967, **1478**, 3842–3845.

27. Y. Gogotsi, A. Nikitin, H. Ye, W. Zhou, J. E. Fischer, B. Yi, H. C. Foley, and M. W. Barsoum, *Nat Mater*, 2003, **2**, 591–594.

28. N. Shimodaira and a. Masui, *J. Appl. Phys.*, 2002, **92**, 902–909.

29. X. Xu, H. Tan, K. Xi, S. Ding, D. Yu, S. Cheng, G. Yang, X. Peng, A. Fakeeh, and R. V. Kumar, *Carbon N. Y.*, 2015, **84**, 491–499.

30. Y. Wang, J. Cao, Y. Zhou, J.-H. Ouyang, D. Jia, and L. Guo, *J. Electrochem. Soc.*, 2012, **159**, A579.

31. J. Liang, Y. Jiao, M. Jaroniec, and S. Z. Qiao, *Angew. Chemie Int. Ed.*, 2012, **51**, 11496–11500.

32. S.-A. Wohlgemuth, R. J. White, M.-G. Willinger, M.-M. Titirici, and M. Antonietti, *Green Chem.*, 2012, **14**, 1515–1523.

33. K. S. W. Sing, *Pure Appl. Chem.*, 1985, **57**, 603–619.

34. M. Kruk and M. Jaroniec, *Chem. Mater.*, 2001, **13**, 3169–3183.

35. S. Goriparti, E. Miele, F. De Angelis, E. Di Fabrizio, R. Proietti Zaccaria, and C. Capiglia, *J. Power Sources*, 2014, **257**, 421–443.

36. B. Guo, X. Wang, P. F. Fulvio, M. Chi, S. M. Mahurin, X. G. Sun, and S. Dai, *Adv. Mater.*, 2011, **23**, 4661–4666.

37. J. Hou, C. Cao, F. Idrees, and X. Ma, *ACS Nano*, 2015, **9**, 2556–2564.

38. J. Ming, Y. Wu, G. Liang, J.-B. Park, F. Zhao, and Y.-K. Sun, *Green Chem.*, 2013, **15**, 2722–2726.

39. D.-C. Guo, F. Han, and A.-H. Lu, *Chem. – A Eur. J.*, 2015, **21**, 1520–1525.

40. V. Etacheri, C. Wang, M. J. O'Connell, C. K. Chan, and V. G. Pol, *J. Mater. Chem. A*, 2015, **3**, 9861–9868.

Process description

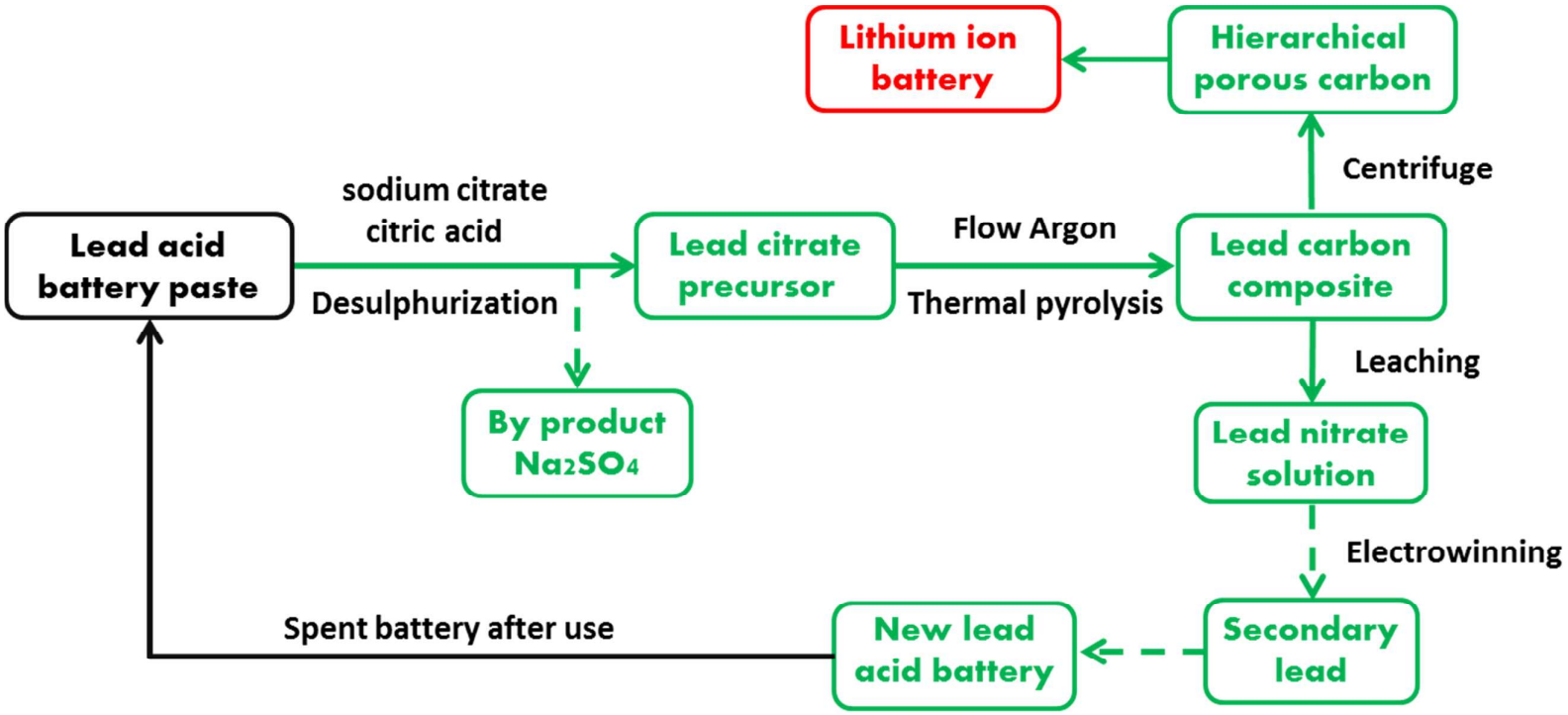

Fig 1.Schematic diagram for the novel battery recycling process

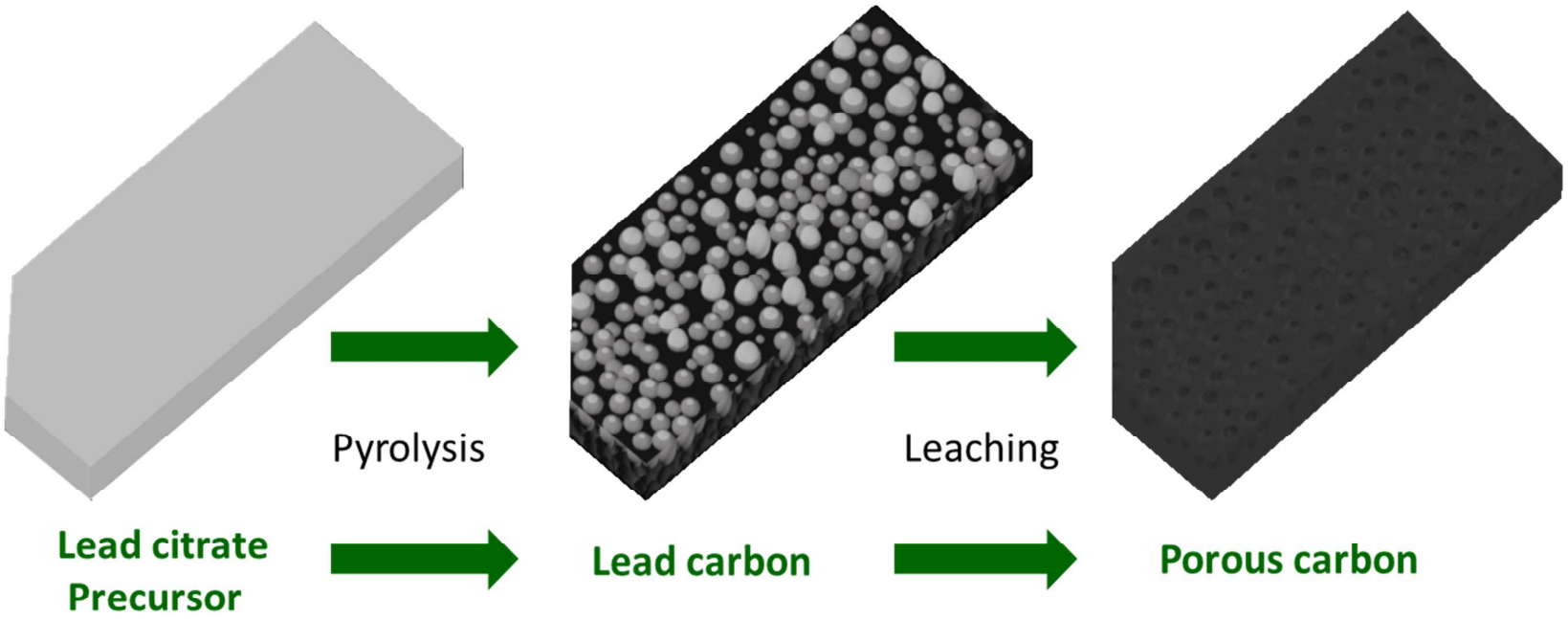

Fig 2.Schematic diagram for the synthesis of functional carbon from lead citrate precursors

Lead citrate precursor characterization

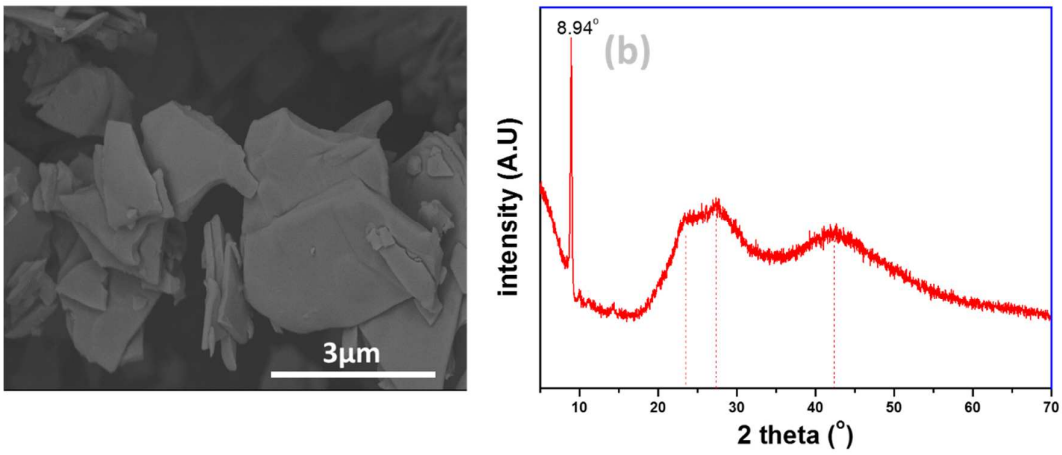

Fig 3. (a) SEM figure and, (b) XRD spectra of the lead citrate precursor

Thermal process

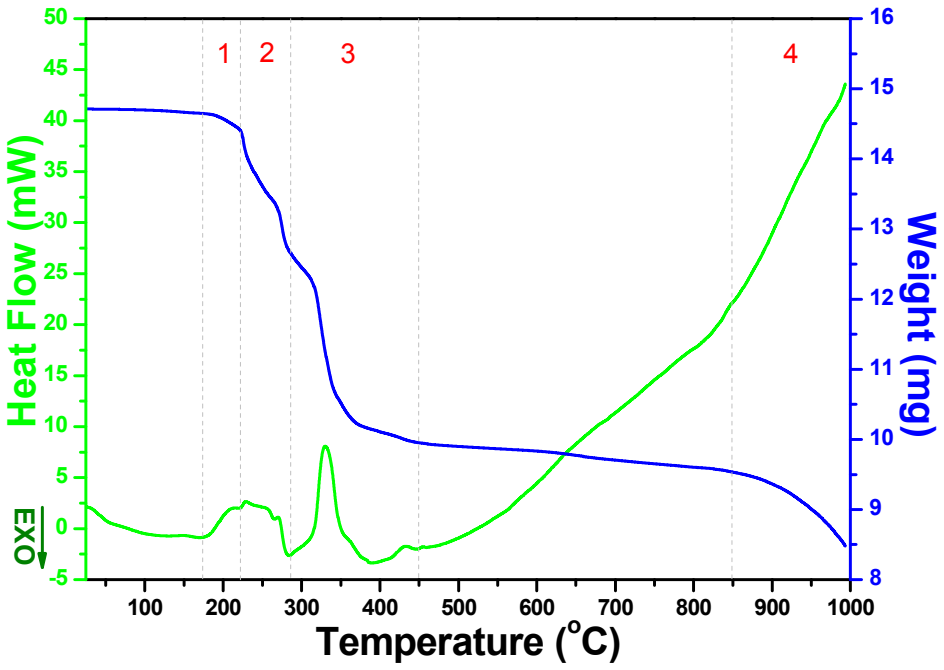

Fig 4. TGA/DSC curves of lead citrate precursors heated in N_2, four decomposition stages labelled in the figure. 1: Lose of crystalline water, 2&3: decomposition of lead citrate, 4: vaporization of metallic lead.

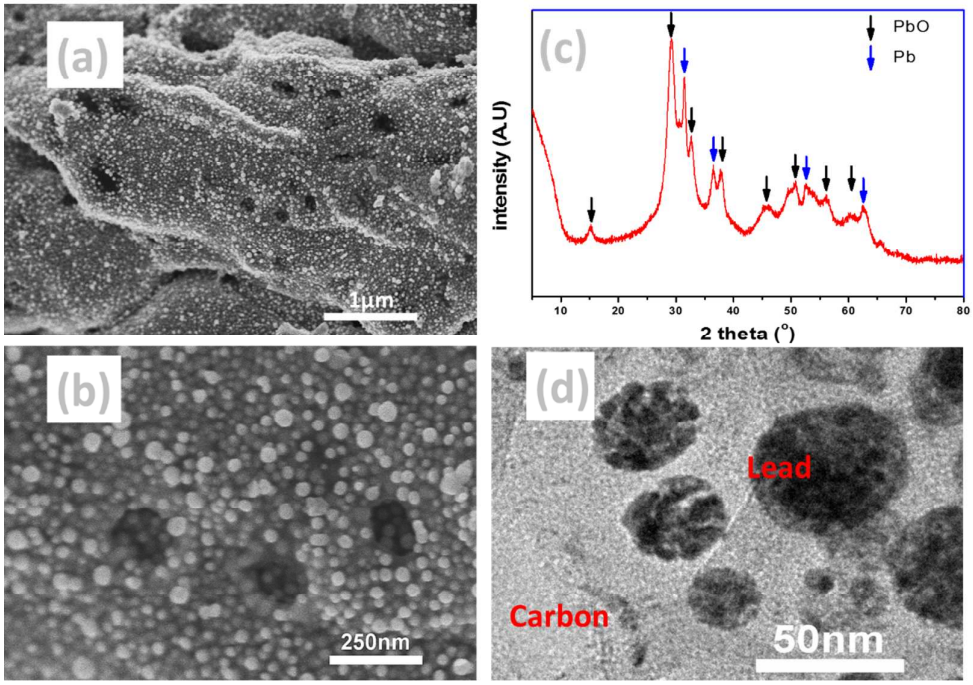

Fig 5.(a)(b) Secondary electron SEM images, (c) XRD spectra and (d) bright field TEM image of 500°C pyrolytic lead carbon composite

Porous carbon characterization

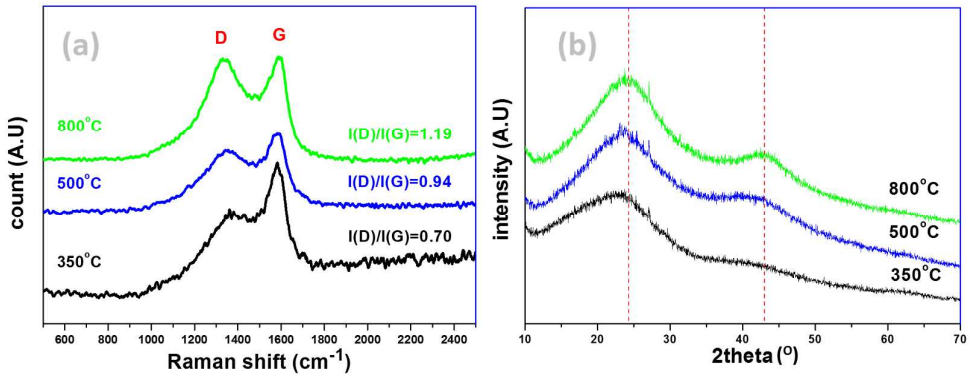

Fig 6. (a) Raman spectra, (b) XRD spectra of porous carbon produced at different temperatures

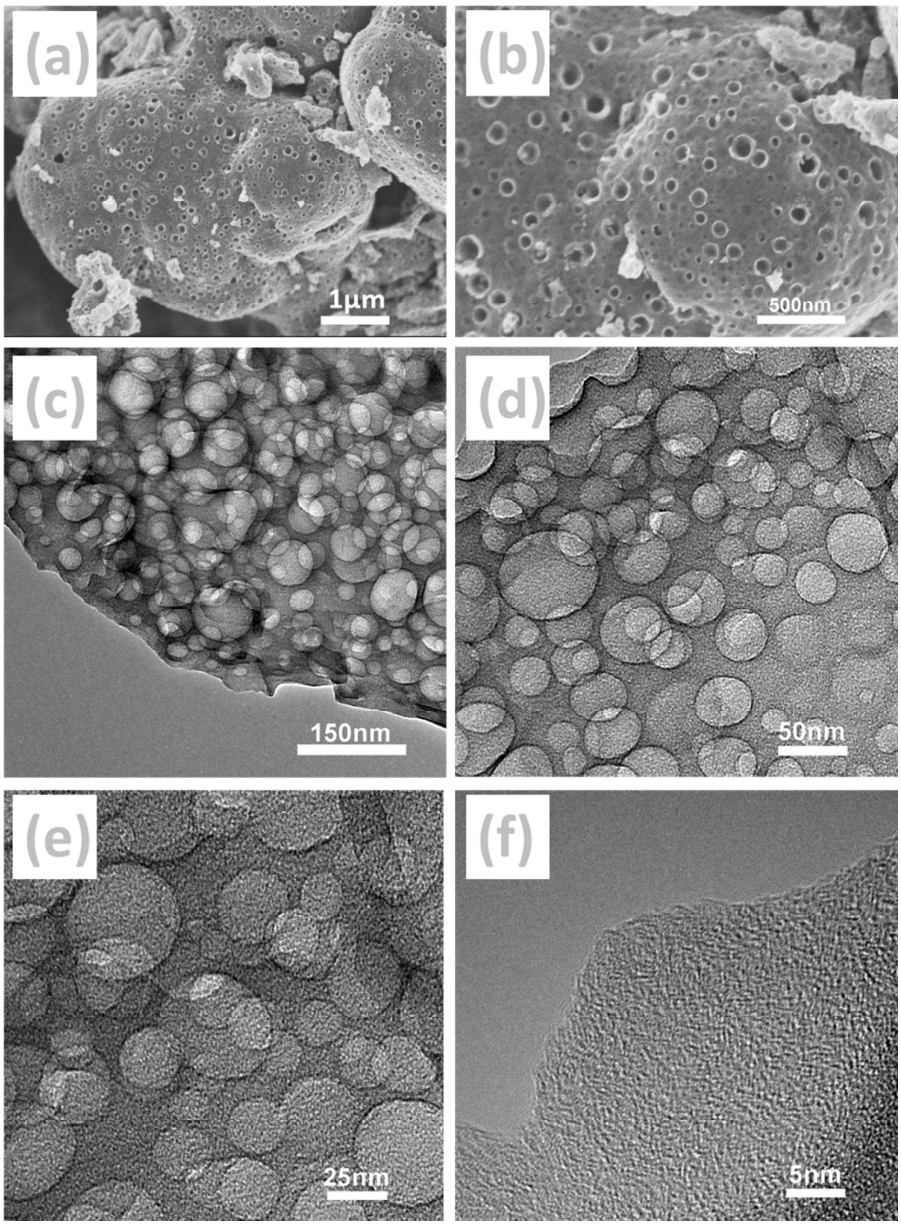

Fig 7. (a)(b) Secondary electron SEM images, and (c-f) bright field TEM images of the carbon derived from lead citrate (500^{o}C)

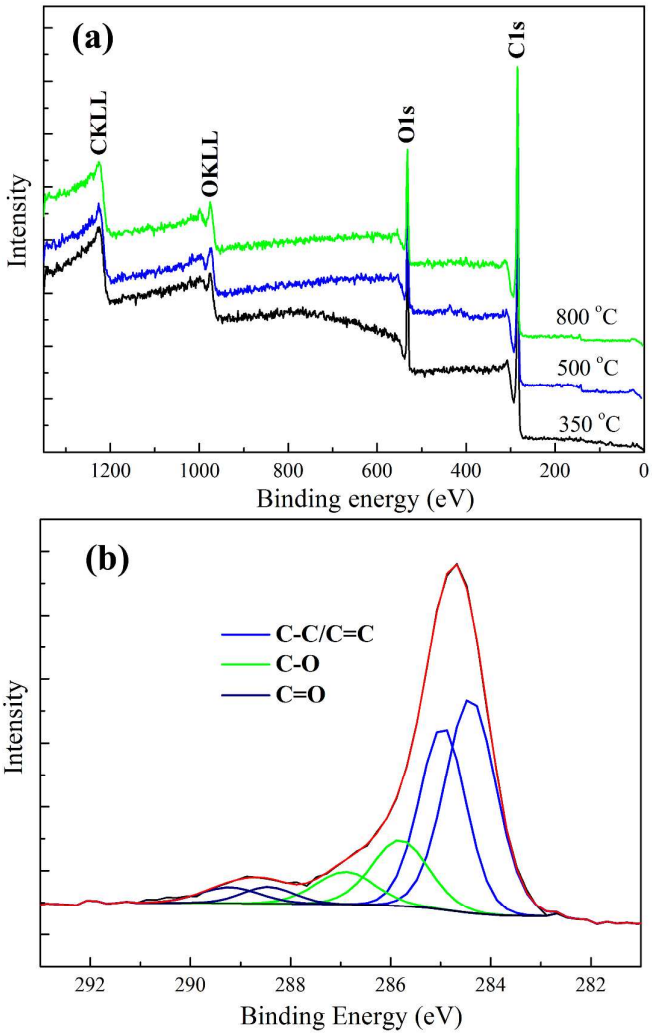

Fig. 8 XPS survey scan (a) of porous carbon produced at different temperatures; high resolution scan of C 1s of the porous carbon treated at the temperature of 500 °C.

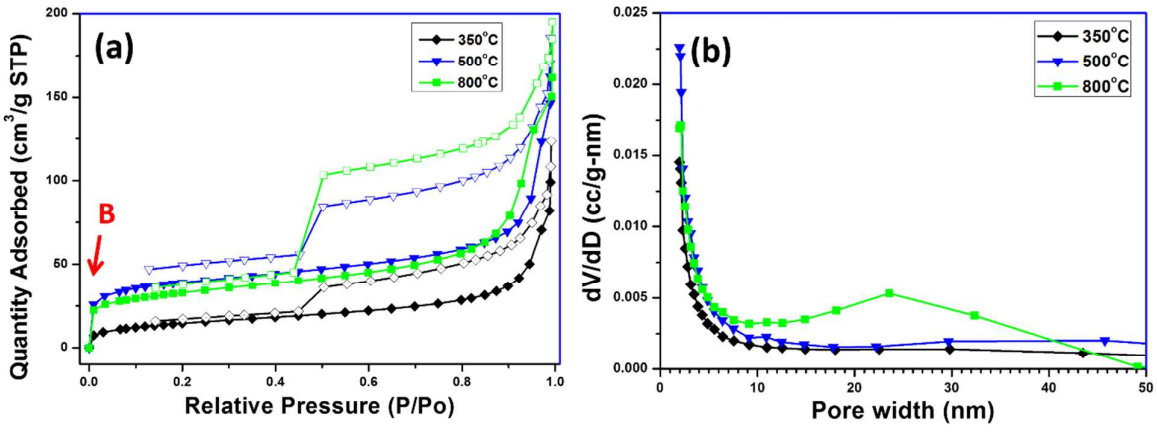

Fig 9. (a) N_2 adsorption-desorption isotherms (solid symbols represent adsorption, open symbols represent desorption), (b) BJH pore size distributions of porous carbon produced at different temperatures.

Table 1: Textural characteristics of porous carbon from different annealing temperature

Treating temperature (^{o}C)	BET surface area[a] ($m^2 g^{-1}$)	Total pore volume ($cm^3 g^{-1}$)	Micropore volume[b] ($cm^3 g^{-1}$)	Mesopore volume[c] ($cm^3 g^{-1}$)	Pore size[d] (nm)
350	52.64	0.1907	0.0000	0.1040	16.25
500	138.51	0.2592	0.0248	0.1561	15.13
800	116.07	0.2865	0.0166	0.2144	15.17

[a] Specific surface area was calculated by the Brunauer-Emmett-Teller (BET) method. [b] micropore volume calculated by t-plot method. [c] mesopore volume calculated by BJH method and N_2 adsorption data for pore diameters between 2 and 50 nm . [d] pore size calculated by BJH method and N_2 adsorption data.

Battery results

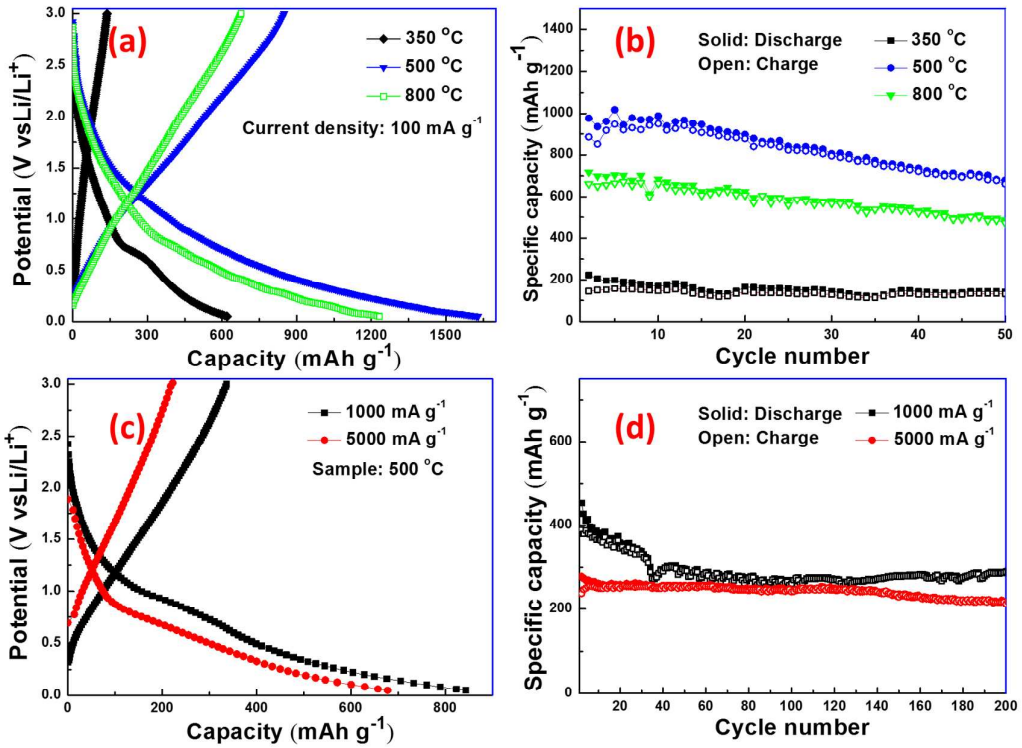

Fig 10. (a) Galvanostatic discharge-charge curves of carbon samples produced at different temperatures at rate of 100mA g^{-1}, (b) cycling performance of carbon samples produced at different temperature at rate of 100mA g^{-1}, (c) Galvanostatic discharge-charge curves of carbon samples carbonized at 500^{o}C at different rates, (d)cycling performance of carbon samples carbonized at 500^{o}C at different rates.